FAILURE CRITERIA FOR COMPOSITE MATERIALS UNDER MULTIAXIAL STRESS STATES

Essam Totry[1], Carlos González[1, 2] and Javier LLorca[1, 2]

[1] Departmento de Ciencia de Materiales, Universidad Politécnica de Madrid.
[2] Instituto Madrileño de Estudios Avanzados en Materiales (IMDEA-Materiales).
E. T. S. de Ingenieros de Caminos. Ciudad Universitaria. 28040 – Madrid, Spain.

ABSTRACT

The potential of computational micromechanics to predict the failure locus of a unidirectional C/PEEK composite subjected to transverse compression and longitudinal shear was established. Numerical simulations were compared with the experimental results of [1], which contain detailed information of the matrix and fiber properties as well as the failure micromechanisms during multiaxial loading. Analyses were based in the finite element analysis of a three-dimensional representative volume element of the lamina microstructure and included the main deformation and failure mechanisms observed experimentally, namely matrix shear yielding and interface decohesion. In addition, the numerical predictions of the failure locus for composites with strong and weak interfaces were compared with those obtained by current phenomenological failure models to establish the accuracy and range of validity of these criteria.

1. INTRODUCTION

Computational micromechanics is emerging rapidly as a very powerful tool to obtain the macroscopic properties of engineering materials from the numerical simulation of the behavior of a representative volume element (RVE) of the microstructure [2]. Applications of this methodology to polymer-matrix composites (PMC) have began to appear recently [3, 4, 5] and they were mainly aimed to study the effect of microstructural factors (fiber orientation, interface strength, etc.) on the onset and progression of damage upon loading. Another interesting application in this field the prediction of the failure locus of PMC lamina subjected to multiaxial stress states, an important and controverted problem. A recent effort to assess the state-of-the-art developments in this matter is the World Wide Failure Exercise [6, 7, 8].

Computational micromechanics stands as a very useful tool in this area as it can provide "virtual tests" which can be used to check the different failure criteria available in the literature. In addition, results of virtual tests are cheaper and free from experimental constrains (buckling, free edge effects, failures at end constraints). However, this methodology should be validated previously against experimental results of PMC lamina subjected to multiaxial stress states and this is the main objective of this paper. To this end, the failure locus of a unidirectional C/ PEEK composite subjected to transverse compression and longitudinal shear was computed and compared with the experimental results of Vogler and Kyriakides [1], which contain detailed information of the matrix and fiber properties as well as the failure micromechanisms during multiaxial loading. The predicted failure locus was compared with the predictions of Puck [9, 10] and LaRC [11] failure criteria and the influence of matrix and interface properties on the accuracy of these criteria was discussed.

2. NUMERICAL MODEL

2.1 Representative volume element of the microstructure

The RVE of the lamina microstructure is a prism, with a square section of dimensions LxL in the 23 plane perpendicular to the fibers (Figure 1). The fiber centers in this plane were generated randomly and sequentially following the strategy of the random sequential adsortion algorithm, as described in

[12]. 30 fibers of 10 μm in diameter were included within the RVE with a volume fraction of 60%. It was assumed that the lamina microstructure was given by an indefinite translation of this RVE along the 2 and 3 axes to eliminate surface effects and, thus, the fiber positions within the RVE kept this periodicity condition. To this end, fibers intersecting the RVE edges were split into an appropriate number of parts and copied to the opposite sides of the square RVE to create the periodic microstructure. Finally, the RVE was extruded along the fiber axis to obtain the three-dimensional prism. The RVE was very thin along the 1 axis (t) because no deformation gradients occur along this axis during transverse compression and longitudinal shear In fact, it was checked that the results of the numerical simulations were independent of the thickness RVE, whose length was only limited by the aspect ratio of the finite elements. Previous simulations of PMC lamina subjected to transverse compression [13] and transverse shear [14] have demonstrated that this size of the RVE is large enough to capture accurately the maximum stress supported by the composite lamina, particularly if the results obtained with various fiber realizations are averaged.
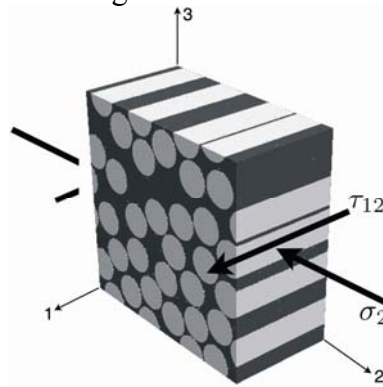

Figure 1: Schematic of the representative volume element of the lamina microstructure subjected to transverse compression (σ_2) and longitudinal shear (τ_{12}).

2.2 Finite element model

The prismatic RVE was discretized for the analysis with the finite element method. The model volume (matrix and fibers) was meshed using modified quadratic 10-node tetrahedra (C3D10M in Abaqus [15]) using an adaptive automatic meshing algorithm. In order to take into account the effect of interface fracture on the composite response, interface elements were included between matrix and fibers throughout the model. The interface element is made up of two quadratic (6-node) triangular surfaces that connect the faces of two adjacent quadratic tetrahedra. The two triangular surfaces of the interface element lie together in the initial configuration (zero thickness) and separate as the adjacent solid elements deform. The relative displacement of the element faces generate normal and shear stresses depending on the constitutive equation of the cohesive crack, which is independent of the element formulation. The interface elements are compatible with C3D10M solid elements in Abaqus [15] and were programmed as a UEL subroutine. The element formulation is detailed in [16] and not repeated here.

Periodic boundary conditions were applied to the RVE surfaces to ensure continuity between neighboring RVEs (which deform like jigsaw puzzles). The periodic boundary conditions can be expressed in terms of the displacement vectors $\vec{U}_1$, $\vec{U}_2$ and $\vec{U}_3$ which relate the displacements between opposite faces according to:

$$\vec{u}(0,x_2,x_3) - \vec{u}(t,x_2 x_3) = \vec{U}_1 \tag{1}$$

2

$$\vec{u}(x_1,0,x_3) - \vec{u}(x_1,L,x_3) = \vec{U}_2 \qquad\qquad (2)$$

$$\vec{u}(x_1,x_2,0) - \vec{u}(x_1,x_2,L) = \vec{U}_3. \qquad\qquad (3)$$

Combined uniaxial compression along the x_2 axis and longitudinal shear along the fibers (σ_2 and τ_{12}, Figure 1) are imposed with $\vec{U}_2 = (\delta_s, -\delta_c, 0)$, where δ_c and δ_s stand for the imposed compressive and shear displacements, respectively. The components of $\vec{U}_1$ and $\vec{U}_3$ are chosen so that the all the normal and shear forces acting on the RVE surfaces are zero (besides those corresponding to transverse compression and longitudinal shear). The compressive and shear strains are given by $\varepsilon_2 = \ln\{1 - \delta_c/L\}$ and $\gamma_{12} = \arctan\{\delta_s/(L - \delta_c)\}$, respectively. The corresponding normal and shear stresses were computed from the resultant normal and tangential forces acting on the RVE faces divided by the actual cross-section. Simulations were carried out with Abaqus/Standard A08 within the framework of the small deformation/displacement theory because the emphasis was in the composite strength, which was normally attained at strains below 7%. Moreover, it was checked in selected cases that simulations carried out within the framework of finite deformations theory provided equivalent results. The average finite element model comprised approximately 25000 elements and 55000 nodes.

2.3 Constitutive equations of matrix, fibers and interface

Carbon fibers were modeled as linear, thermo-elastic transversally isotropic solids and their elastic constants are given in Table 1. The epoxy matrix was assumed to behave as an isotropic, elasto-plastic solid and the elastic constants are given in Table 2. Plastic deformation was governed by the Mohr-Coulomb criterion and the total matrix strain was given by the addition of the elastic and plastic strain components. The Mohr-Coulomb criterion assumes that yielding takes place when the shear stress acting on a specific plane, τ, reaches a critical value, which depends on the normal stress σ_n acting on that plane and takes into account the influence of the triaxiality on the shear yielding of polymers. More details about the numerical implementation of the Mohr-Coulomb model can be found in [18, 19].

Quinson *et al.* [20] measured the yield point of various glassy polymers subjected to different triaxiality levels (uniaxial tension and compression, simple shear and plane strain compression) and reported friction angles in the range 7° to 15°. They are in agreement with the magnitude of 15° obtained from the deviation of the fracture plane from the maximum shear stress plane in FRP subjected to transverse compression [5, 9] and thus $\Phi= 15°$ was chosen for the PEEK matrix in this investigation. Regarding to the yield stress under pure shear, Vogler and Kyriakides [1] carried out tests of the neat PEEK matrix but indicated that the inelastic matrix properties within the composite were different [21], and this has been corroborated recently through nanoindentation [22]. Thus, in absence of accurate data, the matrix cohesion c was chosen equal to 79.5 MPa, the strength of the composite in shear. This hypothesis takes into account that failure under longitudinal shear occurs through the matrix in agreement with the experimental observations [1].

E_1	$E_2 = E_3$	$v_{12} = v_{13}$	v_{23}	$G_{12} = G_{13}$
(GPa)	(GPa)			(GPa)
214	26	0.280	0.445	112

Table 1: Fiber elastic constants (from [17])

Fiber/matrix interfaces were simulated through a cohesive crack model. In the absence of damage, the interface behavior was linear with an initial stiffness K_i (10^5 GPa), which is a numerical parameter large enough to ensure the displacement continuity at the interface and to avoid any modification of the

stress fields around the fibers in the absence of damageDescribed in [16].

E	ν
(GPa)	
4.10	0.356

Table 2: Matrix elastic constants (from [17])

3. RESULTS

Six different fiber realizations were generated to build the corresponding RVEs and meshed following the methodology presented in the previous section. The mechanical response was computed under transverse compression, longitudinal shear and biaxial compression and shear using a pseudo-radial loading path in which $\delta_s/\delta_c = -6$. The corresponding stress-strain curves for pure compression and shear are plotted in Fig. 2(a), while those for biaxial compression and shear are plotted in Fig. 2(b). The strength of the composite lamina in compression was slightly higher than that of the unreinforced matrix, Y_C^m, which was computed in accordance with the Mohr-Coulomb model. Different fiber realizations led variations in the composite strength under uniaxial compression but the maximum difference was below 7% of the compressive strength. Thus, the average value from the six realizations could be considered as a very good approximation of the compressive strength. The specimens deformed in uniaxial compression failed by the development of a plastic shear band in the matrix, which was approximately oriented at 50°- 55° with the pependicular to the loading axis, in agreement with the experimental observations [1, 5]. (Fig. 3(a)). Decohesions at the fiber/matrix interface were observed in several fibers around the shear band but they appeared after the shear band was formed and thus were a consequence of the strain localization rather than the origin. Obviously, the scatter in the stress-strain curves among different RVEs increased in the post-peak regime because the behavior was controlled by the path and orientation of the shear band in the matrix.
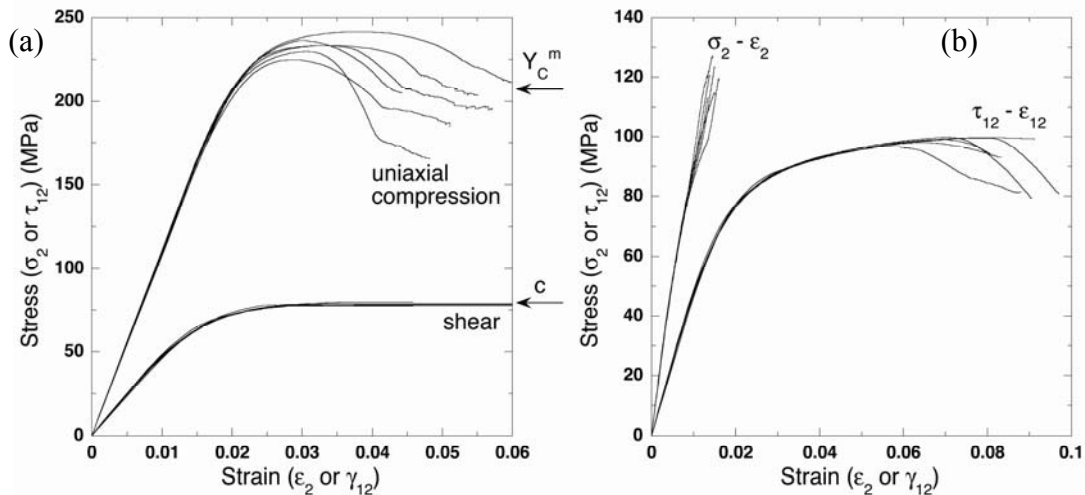

Figure 2: Stress-strain curves of six different RVEs. (a) Uniaxial compression and shear. (b) Biaxial compression and shear using a pseudo-radial loading path characterized by $\delta_s/\delta_c= -6$. The absolute value of the compressive stresses and strains are used in the plots.
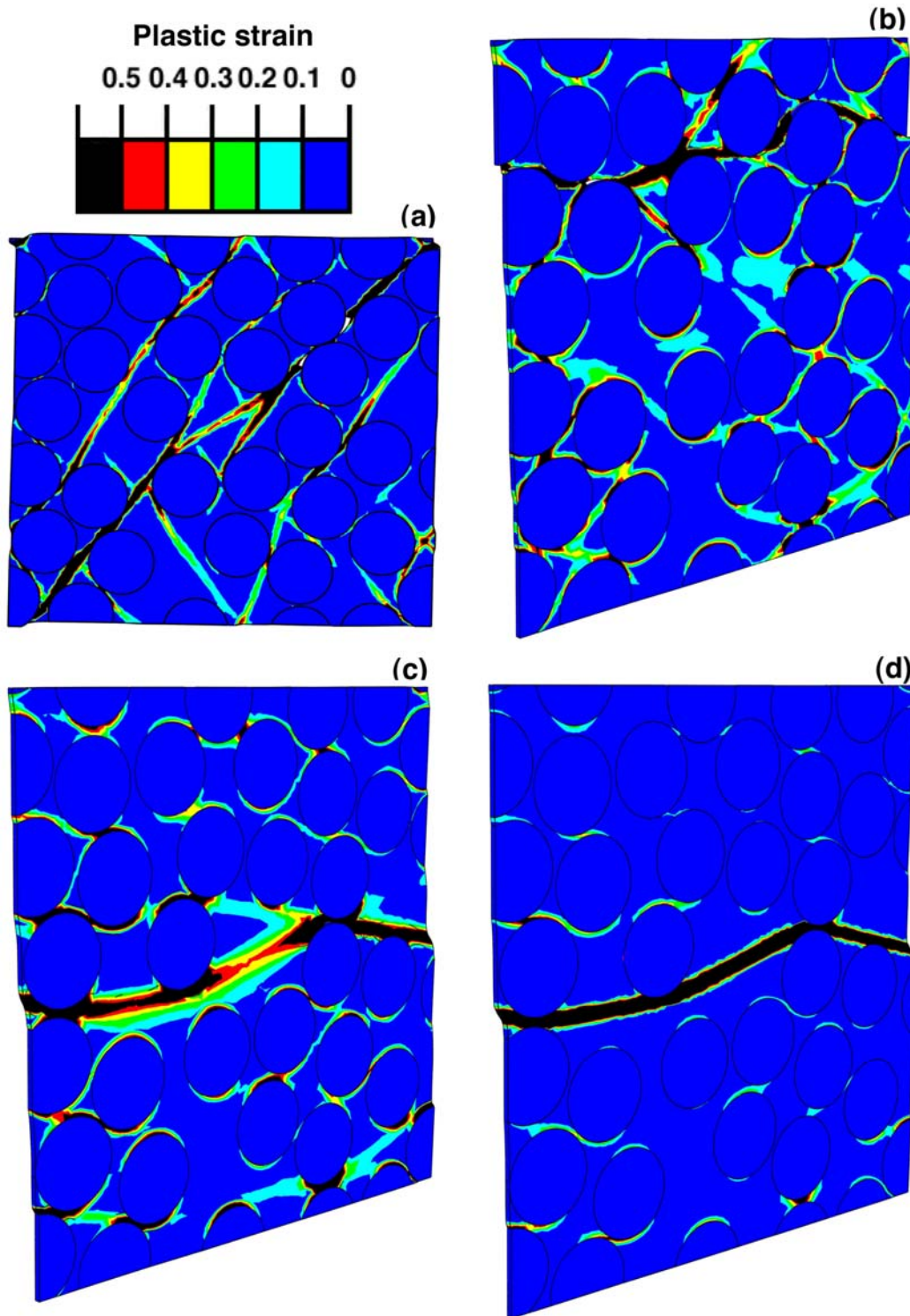
Figure 3: Contour plot of the accumulated plastic strain in the lamina subjected to: (a) uniaxial compression, $\varepsilon_2 = -4.6\%$. (b) Biaxial compression and shear using a pseudo-radial loading path characterized by $\delta_s/\delta_c = -3$, $\varepsilon_2 = -2.5\%$, $\gamma_{12} = 7.4\%$. (c) Biaxial compression and shear using a pseudo-radial loading path characterized by $\delta_s/\delta_c = -6$, $\varepsilon_2 = -1.2\%$, $\gamma_{12} = 7.4\%$. (d) Longitudinal shear. $\gamma_{12} = 5\%$. All plots correspond to the instant of maximum stress in stress-strain curves of Figure 2. Compression is always in the vertical direction.

On the contrary, the stress-strain curves of the six realizations under longitudinal shear were practically superposed and presented a wide plateau, which showed that the composite deformed at a constant shear stress equal to the matrix flow stress in shear, c. The corresponding deformation pattern can be found in the contour plot of the accumulated plastic strain in the matrix in Fig. 3(d). Deformation was initially localized in a matrix band parallel to the applied shear stress τ_{12} and further loading only increased the shear strain in the band. Comparison among the different RVEs showed that the localization occurred along the shortest matrix path parallel to applied shear stress. Once the band percolated through the RVE, deformation continued at a constant shear stress equal to the matrix cohesion. This deformation micromechanism is in perfect agreement with the experimental observations, which reported that the specimens loaded in longitudinal shear failed by splitting along the fibers. Our constitutive equation for the matrix did not take into account the matrix failure in shear and thus it was not possible to reproduce the final fracture of the lamina under these conditions, though this was not necessary as the focus of the simulations was in the maximum strength.

The stress-strain curves for six different RVEs subjected to compression and shear using a pseudo-radial loading path characterized by $\delta_s/\delta_c = -6$ also showed very little scatter (Fig. 2(b)). Failure occurred by the development of a shear band in the matrix parallel to the applied shear stress (Fig. 3(c)), as in the specimens subjected to uniaxial shear. Nevertheless, the compressive stresses led to a more diffuse damage pattern in the matrix and increased the matrix resistance to shear yielding. As a result, the $\tau_{12} - \gamma_{12}$ curves showed strain hardening and presented a well-defined maximum in strength which was followed by the localization of the deformation in continuous band throughout the RVE.

The behavior of the lamina subjected to different biaxial loading paths characterized by δ_s/δ_c is plotted in Figure 4(a) in the $\sigma_2 - \tau_{12}$ stress space. Normal and tangential stresses increased proportionally during elastic deformation upon pseudo-radial deformation and this proportionally disappeared with the onset of plastic deformation in the matrix. Two different failure modes were observed. If $\delta_s/\delta_c \leq -4$, the composite failed in shear-dominated mode and deformation was localized in matrix band parallel to the shear stress. It should be noted that the maximum shear strength increased with the compressive stress applied to the lamina while this failure mode was dominant, in agreement with the postulates of the Mohr-Coulomb model. The compressive stresses became dominant as $\delta_s/\delta_c > -2$ and fracture occurred through a matrix plane whose inclination with respect to the line perpendicular to the compressive stress was in the range 50° - 55°, depending on the details of the spatial arrangement of the fibers. The transition between both mechanisms was found at $\delta_s/\delta_c \approx -3$, in which the orientation of the fracture surface was in between the behavior dominated by shear or compression, as shown in Fig. 3(b).

The predictions of the failure locus under transverse compression and longitudinal shear obtained by computational micromechanics are plotted in Fig. 4(b) together with the experimental results of Vogler and Kyriakides [1]. The agreement is excellent for the whole shape of the failure locus and it is worth noting the experimental points in Fig. 4(b) should be interpreted as lower bounds of the actual strength under shear-dominated fracture because of the end plate effects [1]. It should be noted that the differences between the numerical results and the experiments in the region of shear-dominated failure may also appear because the friction angle chosen for the matrix in the simulations ($\Phi = 15^{\circ}$) was slightly higher than the actual one. The numerical simulations explained the transition from shear failure by splitting along the fibers to compressive failure along an inclined surface parallel to the fibers. The former is characterized by a linear increase of the shear strength with the applied compressive stress and the slope depends of the friction angle Φ. The end of this regime is accompanied by a change in the failure mode to compressive failure, leading to a gentle reduction in the maximum shear strength at failure.
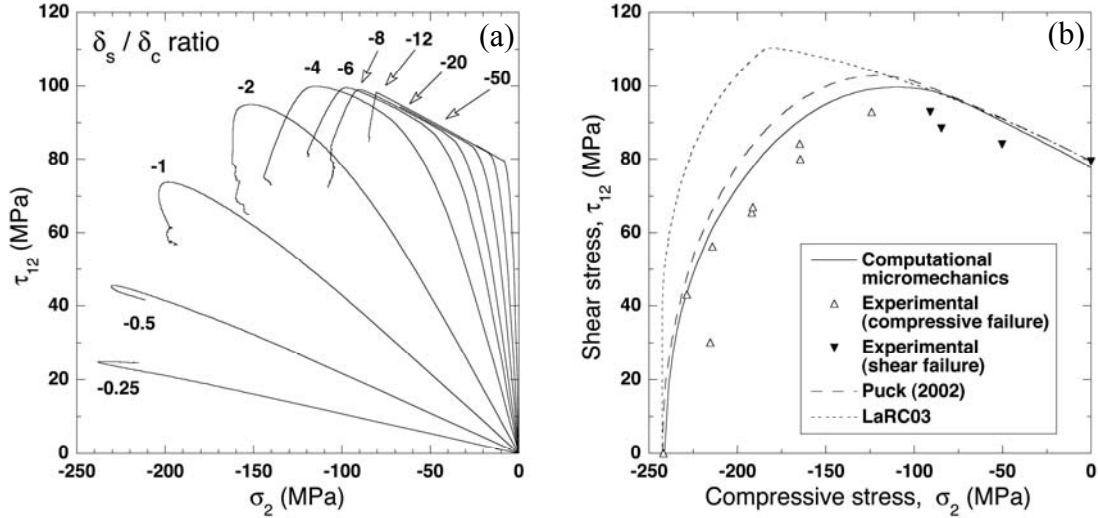
Figure 4: a) Mechanical response of the composite lamina under biaxial deformation in the $\sigma_2 - \tau_{12}$ stress space. The corresponding δ_s/δ_c ratio for each curve is given in the figure. b) Failure locus under transverse compression and longitudinal shear. Experimental results [1] and numerical simulations using computational micromechanics as well as predictions of the Puck [10] and LaRC03 models [23]

The corresponding failure envelopes corresponding to the Puck [10] and LaRC03 [23] models are also plotted in Fig. 4(b) for comparison. Both models assume that the composite lamina is isotropic in the 23 plane and that failure under transverse compression and longitudinal shear occurs through surfaces parallel to the fibers. Fracture is caused by the normal and tangential stresses acting on the fracture plane following the Mohr-Coulomb criterion (matrix-dominated failure). The failure surface is determined by computing the critical orientation of the fracture plane for each combination of normal and tangential stresses. The two models differ slightly in their expression of the Mohr-Coulomb failure criterion. Puck [9, 10] proposed

$$(\frac{\tau_t}{S_T - \eta_t\sigma_n})^2 + (\frac{\tau_l}{S_L - \eta_l\sigma_n})^2 = 1 \tag{4}$$

where τ_t and τ_l are, respectively, the transverse and longitudinal shear stresses and σ_n is the normal stress acting on the fracture plane. S_L and S_T stand for the lamina strength under longitudinal and transverse shear. S_L can be measured directly in the laboratory but mechanical tests under transverse (out-of-plane) shear are very difficult to carry out and S_T is normally from the transverse compressive strength of the lamina Y_C by assuming the failure is controlled by the matrix and follows the Mohr-Coulomb model.

The failure locus can be determined by computing the critical orientation of the fracture plane for each combination of normal and tangential stresses once the lamina properties under longitudinal shear and transverse compression are given [10].

Dávila et al. [23] followed a similar strategy to obtain the failure locus under transverse compression and longitudinal shear starting from another approximation based on the Mohr-Coulomb model,

$$(\frac{|\tau_t| + \eta_t \sigma_n}{S_T})^2 + (\frac{|\tau_l| + \eta_l \sigma_n}{S_L})^2 = 1 \qquad (5)$$

which assumes that the compressive stresses acting on the fracture plane reduce the effective shear stresses rather than increase the shear strength.

Both models (Puck and LaRC03) reproduce adequately the two main failure mechanisms (compressive and shear-dominated failure) which were found in the experiments and in the numerical simulations. Nevertheless, the Puck model is able to predict accurately the failure surface in the whole range of biaxial stresses. On the contrary, LaRC03 criteria does not capture adequately the transition between both failure mechanisms and tends to overestimate the composite strength.

4. CONCLUSIONS

The mechanical response of a composite lamina made up of PEEK matrix unidirectionally reinforced with 60 vol. % C fibers subjected to transverse compression and longitudinal shear was simulated using computational micromechanics. The failure locus --- given by the envelope of the loading curves under different biaxial loading conditions in the σ_2 - τ_{12} stress space --- was in excellent agreement with the experimental results reported by Vogler and Kyriakides [1] for this material. In addition, the transition from shear to compression-dominated fracture and the differences in the orientation of the fracture plane were adequately predicted by the numerical simulations. These results demonstrate the actual potential of computational micromechanics to predict the macroscopic properties of composite lamina from the properties and spatial distribution of the constituents.

The numerical simulations were also useful to establish the range of validity of current failure criteria for composites. In particular, they showed that Puck failure criterion [10] provides an excellent estimate for the failure locus of unidirectional laminates subjected to transverse compression and longitudinal shear when fracture is controlled by the matrix. The failure loci obtained from the computational micromechanics can be very useful in extending the accuracy of current failure criteria for conditions of interface dominated failure.

REFERENCES

1- T. J. Vogler, S. Kyriakides, "Inelastic behavior of an AS4/PEEK compoiste under combined transverse compression and shear. Part I: experiments", *International Journal of Plasticity*, (1999);15:783-806.

2- T. I. Zohdi, P. Wriggers, "Introduction to Computational Micromechanics", *Springer*, 2005.

3- A.Miravete, J.M. Bielsa, A.Chiminelli, J.Cuartero, S.Serrano, N.Tolosana, R.G. de Villoria, "3D mesomechanical analysis of three-axial braided composite materials", *Composites Science and Technology* (2006);66 :2594-2964.

4- S. Song, A. M. Waas, K. W. Shahwan, X. Xiao, O. Faruque, "Braided textile composites under compressive loads. modeling the response, strength and degradation", *Composites Science and Technology*, (2007);67:3059-3070.

5- C. González, J. LLorca, "Mechanical behavior of unidirectional fiber-reinforced polymers under transverse compression: microscopic mechanisms and modeling", *Composites Science and*

Technology, (2007);67:2795-2806.

6- M. J. Hinton, P. D. Soden, A. S. Kaddour, "Failure criteria in fiber-reinforced polymer composites": *the World Wide Failure exercise*, Elsevier, 2004.

7- P. D. Soden, M. J. Hinton, A. S. Kaddour, "A comparison of the predictive capabilities of current failure theories for composite laminates", *Composites Science and Technology*, (1998);58:1225-1254.

8- A. S. Kaddour, M. J. Hinton, P. D. Soden, "A comparison of the predictive capabilities of current failure theories for composite laminates: additional contributions", *Composites Science and Technology*, (1998);58:1225-1254.

9- A. Puck, H. Schürmann, "Failure analysis of FRP laminates by means of physically based phenomenological models", *Composites Science and Technology*, (1998);58:1045-1067.

10- A. Puck, H. Schürmann, "Failure analysis of FRP laminates by means of physically based phenomenological models", *Composites Science and Technology*, (2002);62:1633-1662.

11- S. T. Pinho, C. G. Dávila, P. P. Camanho, L. Iannucci, P. Robinson, "Failure models and criteria for FRP under in-plane of three-dimensional stress states including shear non-linearity", Report NASA/TM-2005-213530, 2005.

12- J. Segurado, J. LLorca, "A numerical approximation to the elastic properties of sphere-reinforced composites", *Journal of the Mechanics and Physics of Solids*, (2002);50:2107-2121.

13- C. González, J. LLorca, "Numerical simulation of the fracture behavior of Ti/SiC composites between $20^{o}C$ and $400^{o}C$", *Metallurgical and Materials Transactions A*, (2007);38:169-179.

14- E. Totry, C. González, J. LLorca, "Failure locus of fiber-reinforced composites under transverse compression and out-of-plane shear", *Composites Science and Technology*, (2008);68 :829--839.

15- Abaqus, Users' Manual, version 6.7, ABAQUS, Inc., 2008.

16- J. Segurado, J. LLorca, "A new three-dimensional interface finite element to simulate fracture in composites", *International Journal of Solids and Structures*, (2004);41:2977-2993.

17- S. Y. Hsu, T. J. Vogler, S. Kyriakides, "Inelastic behavior of an AS4/PEEK compoiste under combined transverse compression and shear. Part II: modeling", *International Journal of Plasticity*, (1999);15:807-836.

18- Abaqus, Theory Manual, HKS, Inc., 1998.

19- P. Menetrey, K. J. Willam, "Triaxial failure criterion for concrete and it generalization", *ACI Structural Journal*, (1995);92:311-318.

20- R. Quinson, J. Perez, M. Rink, A. Pavan, "Yield criteria for amorphous glassy polymers", *Journal of Materials Science*, (1997);32:1371-1379.

21- S. Y. Hsu, T. J. Vogler, S. Kyriakides, "Compressive strength predictions for fiber composites", *Journal of Applied Mechanics*, (1998);65:7--16.

22- J. R. Gregory, S. M. Spearing, "Nanoindentation of neat and in situ polymers in polymer-matrix composites", *Composites Science and Technology*, (2005);65:595-607.

23- C. Dávila, P. P. Camanho, C. A. Rose, "Failure criteria for FRP laminates", *Journal of Composite Materials*, (2005);39:323-345.